Chapter 3

A Current Sensor Based Adaptive Step-Size MPPT With SEPIC Converter for PV Systems

3.1 Introduction

Photovoltaic (PV) power generation is commonly used as renewable energy source because of the advantages, e.g. pollution free, noiseless, lesser maintenance and easy to install in distributed fashion and in varied sizes [70, 71]. The output of PV module depends on operating conditions, such as PV-cell temperature and insolation-level [72, 73]. Researchers developed various techniques to extract maximum power from the PV sources. Some of the MPPT techniques are perturb and observe (P&O) [20,74,75], hill climbing (HC) [76], incremental conductance (IncCond) [30,77], fractional voltage/current MPPT control [78], fuzzy-logic (FL) [39, 79], neural network (NN) [44, 80], optimization techniques [50], and sliding mode (SM) control [81–83].

Among the conventional MPPT techniques, P&O and the IncCond techniques are widely used due to their simplicity yet being efficient [84]. A demerit of P&O like algorithms is that it drifts away from MPP [20] for sudden changes in insolation leading to lesser efficiency. In [36], the drift problem is presented and resolved by modified P&O algorithm. Other machine learning MPPT techniques, e.g. NN [44], FL [79], SM [81], and optimization techniques, show improved performance. But these are not commonly used due to need of expensive controllers and complexity for implementation and big data

processing for the training of the system to enhance the tracking accuracy [85].

In conventional MPPT techniques, the perturbation step-size is selected by considering convergence speed and steady-state performance. For faster convergence and to enhance the steady-state response, an adaptive step-size MPPT technique is proposed in [36]. In such adaptive methods, the step-size is a linear function of either the derivative of power to duty-cycle (dP_{pv}/dD) [67] or the derivative of power to voltage (dP_{pv}/dV_{pv}) [68]. This leads to transient performance is improvement by reducing the tracking time. However, most of these methods are applied to voltage sensor based MPPT techniques.

Both the current and the voltage sensors are used for implementing some of the MPPT algorithms, e.g. P&O that leads to increased cost [20, 30, 39, 44, 50, 74–80]. Only a handful of techniques use either a voltage [36, 86] or a current sensor [69]. Only voltage based methods are considerably cheaper as compared to the current based methods due to larger cost involved in current sensing. On the other hand, it is well known that the PV voltage varies logarithmically with solar insolation [19]. It makes all the voltage sensor based MPPTs to be less sensitive for large change in irradiation and hence yields slower convergence (due to large insolation change) when initial point is far away from the MPP. It is otherwise for the current sensing since the PV current varies linearly with insolation level. This property is very useful for a fast current sensor based MPPTs than voltage sensor based one for frequent change in insolation [19, 87].

In the context of choice of converters, several different converters are used for impedance matching to obtain maximum power from the PV systems, e.g. buck [69], boost [71], buck-boost [88], SEPIC [19, 20] converters. The selection of converter topology depends on the PV module voltage and the load voltage [89]. For example, the buck topology is used only for the cases where the PV module voltage is always higher than the load voltage. Similarly, the boost topology is applicable if the PV module voltage is always lower than the load voltage. Clearly, both are extreme ended considering the fact that insolation variation in a day is over a wide range. On the other hand, the drawback of buck-boost converter is that the output is inverted which results in complex sensing and feedback circuit. It also has discontinuous input current that limits the ability of the converter. A comparison of several buck-boost converters from different point of view is given in [18]. Among these, although the SEPIC converter has poor efficiency and higher cost, it still has the merits of non-inverting polarity, continuous input current, works as buck-boost

converter over wide range and low input current-ripple [20]. It is suitable for either voltage or current applications [90, 91]. The main losses in the DC-DC converters are switching losses in the MOSFET and the diode, copper losses in the inductor windings and inductor core losses. A comparison of losses in converters is given in [92], it can be seen that all the converters have same number of switches (MOSFET and diode), hence the switching losses will be the same. The losses in the inductors are lower for the SEPIC converter due to the reduced input current ripple that decreases the peak inductor current though it has two inductors. These properties make SEPIC converter a suitable candidate for PV applications.

In this chapter, SEPIC converter is used for development of a new MPPT technique, which is realized using a single current sensor. A hall-effect current sensor is used for current sensing, which has many advantages like excellent accuracy and linearity, wide frequency bandwidth, optimized response time, lesser temperature drift, high resistance to external noise and current overload capacity. A new variable step-size algorithm is developed that yields a large step-size when the operating point is away from MPP. This results in faster convergence for change in MPP. An experimental setup is developed for the implementation of the Proposed MPPT technique and an ARDUINO UNO micro-controller is used for the programming of algorithm.

A 40 W PV panel is considered for simulation and experiment. It has uses in stan-dalone applications, such as solar lantern, solar mobile charger, small solar battery banks, solar garden lights, solar street light etc. It can also be used as portable power supply. It is shown through simulation and experimental results that the proposed algorithm yields improved convergence time and thereby improves the efficiency of the system.

3.2 The Linearity of PV Current with Insolation

A single-diode electrical equivalent circuit [93] is well known for modeling of PV modules. The V-I relationship of a PV-module is given by (3.1).

$$I_{pv} = I_p - I_{rs}\left[exp\left(\frac{V_{pv} + I_{pv}R_{se}}{n_s b v_t}\right) - 1\right] - \frac{V_{pv} + I_{pv}R_{se}}{R_p} \tag{3.1}$$

where V_{pv} and I_{pv} are the output voltage and current of the PV-module, respectively. I_{rs} is the reverse saturation current, R_{se} and R_p are the series and parallel resistances,

respectively, n_s is the number of series connected PV cells in a module, b is the ideality factor of the diode, $v_t = kT/e$ is thermal voltage, T is module temperature in K, e is charge on electron, and k is the Boltzmann's constant.

For an ideal PV module, the series and parallel resistances in (3.1) are zero and infinite, respectively. Then the voltage-current relationship can be written as:

$$I_{pv} = I_p - I_{rs}\left[exp\left(\frac{V_{pv}}{n_s b v_t}\right) - 1\right] \tag{3.2}$$

where I_p is the photo-current and it is expressed in terms of the insolation G and the PV cell temperature T as follows.

$$I_p = [I_{STC} + k_{isc}(T - T_{STC})]\frac{G}{G_{STC}} \tag{3.3}$$

where k_{isc} is the short circuit current temperature coefficient, I_{STC} is the short circuit current at $G_{STC} = 1000\ W/m^2$, $T_{stc} = 298\ K$.

From (3.2) and (3.3), it is clear that the V_{pv} is nonlinear with G, whereas the PV current I_{pv} depends linearly. Because of nonlinear relation between voltage and solar insolation, the convergence to maximum power point (MPP) is nonlinear for a voltage sensing based algorithm. However, the linear relationship between PV current with G would be beneficial for detecting solar insolation changes irrespective of the insolation level. Due to this, a current based MPPT algorithm can be adopted for uniform convergence over wide range of insolation and the same is studied in this work. It may be noted that linear characteristic is beneficial since uniform convergence can be achieved using simpler logic, whereas intrinsically complex logic is required to tackle nonuniform behavior.

3.2.1 Switching Function for SEPIC Converter

The photovoltaic (PV) system considered is given in Fig. 3.1. A SEPIC converter is used to supply the load form the PV panel. The duty-cycle of the converter is adapted by the MPPT controller for operation at the MPP. The proposed MPPT controller uses only one current sensor for determining the MPP. The corresponding switching function is derived below.

The output voltage of SEPIC converter can be written as

$$V_L = [D/(1 - D)]V_{pv} \tag{3.4}$$

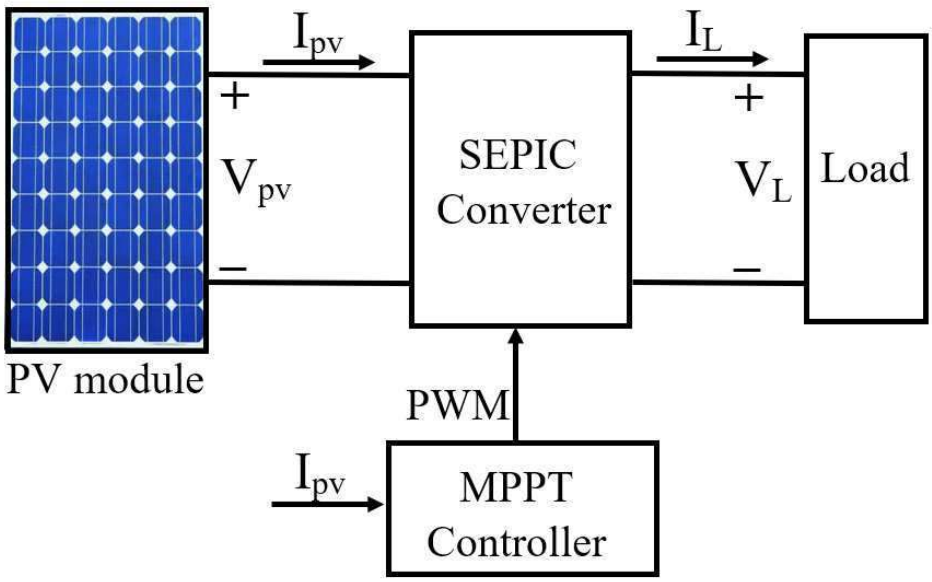

Figure 3.1: PV system with the MPPT controller.

where V_L is the output voltage and D is the duty-ratio of SEPIC converter. The efficiency η of the SEPIC converter can be expressed for a load R_L as

$$\eta = \frac{V_L I_L}{V_{pv} I_{pv}} \tag{3.5}$$

$$\eta = \frac{V_L^2/R}{V_{pv}^2/R_{eq}} = \left(\frac{V_L}{V_{pv}}\right)^2 \frac{R_{eq}}{R_L} = \left(\frac{D}{1-D}\right)^2 \frac{R_{eq}}{R_L} \tag{3.6}$$

where R_{eq} is the equivalent resistance of the converter. Then, R_{eq} can be obtained from equation (4.1) as

$$R_{eq} = \eta \left(\frac{1-D}{D}\right)^2 R_L \tag{3.7}$$

The PV module power P_{pv} can be expressed by using (4.2) as:

$$P_{pv} = I_{pv}^2 R_{eq} = \eta I_{pv}^2 \left(\frac{1-D}{D}\right)^2 R_L \tag{3.8}$$

We can also write

$$P_{pv} = \left(\sqrt{P_{pv}}\right)^2 \tag{3.9}$$

From (3.9), the variation of P_{pv} with respect to the duty ratio D can be written as:

$$\frac{dP_{pv}}{dD} = 2\sqrt{P_{pv}} \left[\frac{d\sqrt{P_{pv}}}{dD}\right] \tag{3.10}$$

By putting the value of P_{pv} from (4.3) into 10, we get

$$\frac{dP_{pv}}{dD} = \left[I_{pv}\left(\frac{-1}{D^2}\right) + \left(\frac{1-D}{D}\right)\frac{dI_{pv}}{dD} \right] 2\sqrt{\eta R_L P_{pv}} \tag{3.11}$$

$$\frac{dP_{pv}}{dD} = \left[\frac{-I_{pv}dD + D(1-D)dI_{pv}}{D^2 dD} \right] 2\sqrt{\eta R_L P_{pv}} \tag{3.12}$$

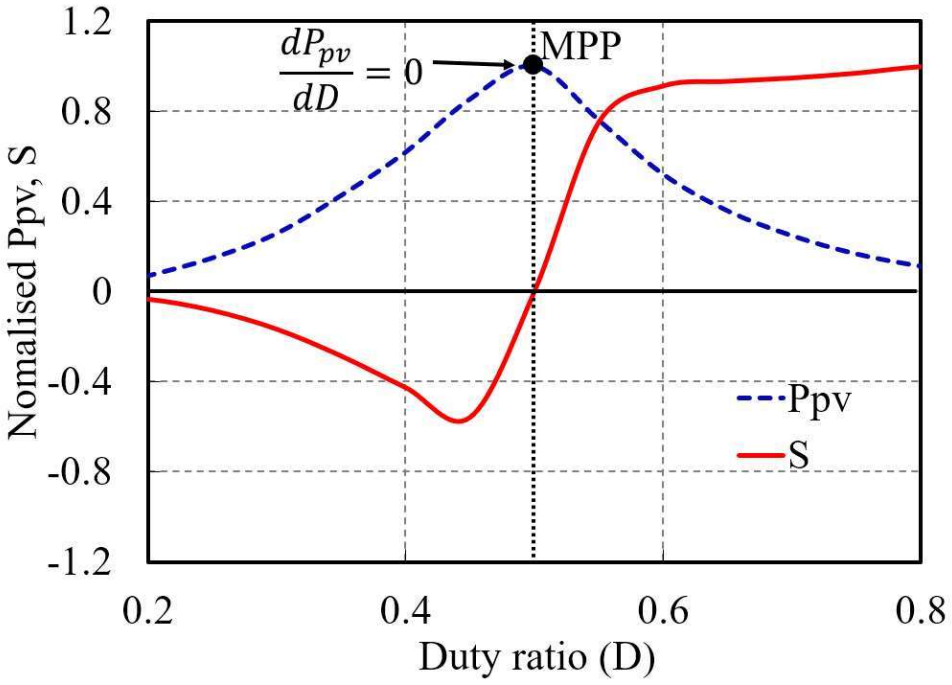

Figure 3.2: Normalized variation of P_{pv}, S for a PV module.

The $P_{pv} - D$ characteristic waveform of a PV module is shown in Fig. 3.2. One can observe that dP_{pv}/dD is equal to zero at the MPP. Furthermore, dP_{pv}/dD is greater than zero to the left of the MPP and dP_{pv}/dD is less than zero to the right of the MPP.

Hence, for maximum power, $dP_{pv}/dD = 0$ and it can be calculated from (4.6) as:

$$D(1-D)dI_{pv} - I_{pv}dD = 0 \tag{3.13}$$

Thereby, the switching function S can be written as the following:

$$S = [D(1-D)dI_{pv} - I_{pv}dD] \begin{cases} > 0, \text{to the right of MPP} \\ = 0, \text{at MPP} \\ < 0, \text{to the left of MPP} \end{cases} \tag{3.14}$$

Note that the right of MPP indicates increased duty-ratio and the left of MPP indicates decreased duty-ratio. Hence, a MPPT controller can be developed based on the sign of switching function S. The corresponding $S - D$ characteristic waveform is also shown in Fig. 3.2. It is clear that S passes through zero at MPP.

3.2.2 Switching Function for Buck Converter

The switching function S for tracking the MPP in case of buck converter can be obtained by evaluating R_{eq} and dP_{pv}/dD as follows

$$R_{eq} = \frac{\eta R_L}{D^2} \tag{3.15}$$

$$P_{pv} = \eta R_L (I_{pv}/D)^2 \tag{3.16}$$

$$\frac{dP_{pv}}{dD} = 2\sqrt{\eta R_L P_{pv}} \left[\frac{D dI_{pv} - I_{pv} dD}{D^2 dD}\right] \tag{3.17}$$

$$S = [D dI_{pv} - I_{pv} dD] \begin{cases} > 0, \text{to the right of MPP} \\ = 0, \text{at MPP} \\ < 0, \text{to the left of MPP} \end{cases} \tag{3.18}$$

3.2.3 Switching Function for Boost Converter

Similarly, the switching function S for tacking the MPP in case of boost converter can be obtained as follows

$$R_{eq} = \eta R_L (1 - D)^2 \tag{3.19}$$

$$P_{pv} = \eta R_L [I_{pv}(1 - D)]^2 \tag{3.20}$$

$$\frac{dP_{pv}}{dD} = 2\sqrt{\eta R_L P_{pv}}[(D - 1) dI_{pv} - I_{pv} dD] \tag{3.21}$$

$$S = [(D - 1) dI_{pv} - I_{pv} dD] \begin{cases} > 0, \text{to the right of MPP} \\ = 0, \text{at MPP} \\ < 0, \text{to the left of MPP} \end{cases} \tag{3.22}$$

From the above, it can be seen that the choice of switching function S depends on the converter type for this current sensor based MPPT technique while the conventional techniques, like P&O is independent of the DC-DC converter topology. However, for a given converter and S is chosen, the remaining of the MPPT algorithm remains the same as described in the next section.

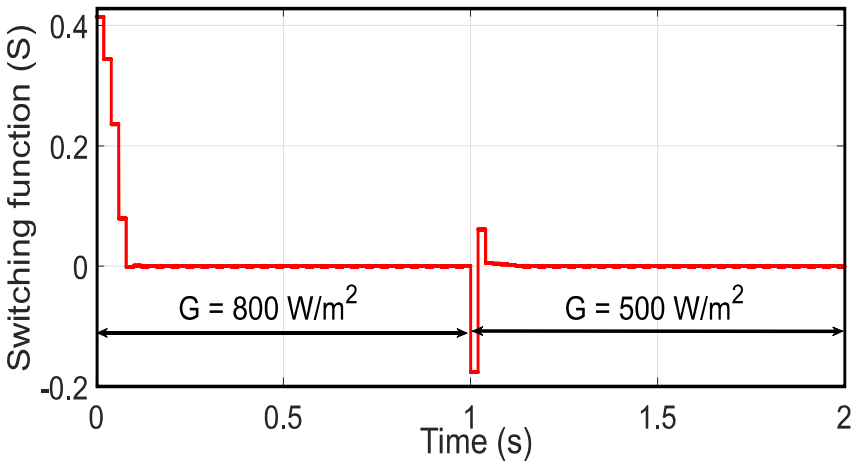

Figure 3.3: Variation of S for a step change in insolation level.

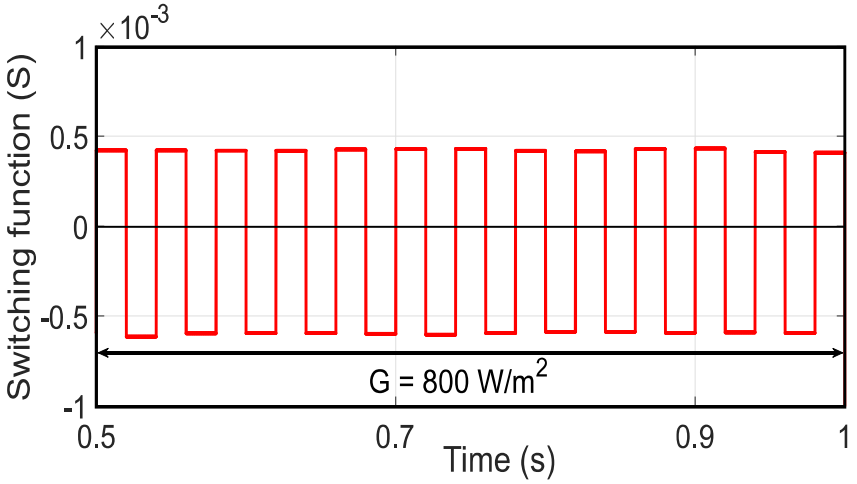

Figure 3.4: Variation of S at steady-state.

3.3 A Novel Adaptive MPPT Technique

A current sensor based MPPT technique using variable perturbation step-size (ΔD) is developed. The values of I_{pv} and D during the present and previous iteration cycle are denoted by $I_{pv}(m)$, $I_{pv}(m-1)$, $D(m)$ and $D(m-1)$, respectively, where m denotes the sampling instant.

The changes in the PV module current I_{pv} and duty-cycle D from previous iteration to the next iteration are obtained as follows.

$$dI_{pv}(m) = I_{pv}(m) - I_{pv}(m-1) \tag{3.23}$$

$$dD(m) = D(m) - D(m-1) \tag{3.24}$$

$$D(m+1) = D(m) \pm \Delta D(m) \tag{3.25}$$

The position of operating point is decided by calculating sign of S. If $S > 0$ then the next duty-cycle $D(m+1)$ is decreased by $\Delta D(m)$, and if $S < 0$ then the next duty-cycle $D(m+1)$ is increased by $\Delta D(m)$ as mentioned in (3.25).

The variation in S is large during transient-state for a change in insolations say from 0 to 800 W/m^2 and from 800 W/m^2 to 500 W/m^2 as shown in Fig. 3.3. Whereas the variation in S is small at steady-state as given in Fig. 3.4. Thus, a FSS scheme is not suitable for MPPT controllers for varying insolation condition. An adaptive perturbation step-size is considered to change the ΔD, which is written in terms of S as

$$\Delta D(m) = \alpha S(m) \mid S(m) \mid \tag{3.26}$$

$$= \alpha S^2(m) Sign(S(m)) \tag{3.27}$$

With

$$\frac{\Delta D_{min}}{S(m) \mid S(m) \mid} \leq \alpha \leq \frac{\Delta D_{max}}{S(m) \mid S(m) \mid} \tag{3.28}$$

where α is a constant to be chosen and $Sign$ is the signum function. The value of α should be calculated based on (3.28). The PV power for different values of α are shown in Fig. 3.5. It can be observed that for α less than 1, the convergence time deteriorates rapidly. For $\alpha \geq 1$, there are little variation in the convergence time. In this work, we have taken $\alpha = 1$. In the right hand side of (3.27), the component $Sign(S(m))$ facilitates the necessary switching towards and around the MPP, whereas $S^2(m)$ generates the adaptive feature in ΔD so that ΔD is large when S is large and otherwise. Hence, it ensures faster

convergence to MPP when S is large. Thus, the proposed MPPT improves the transient response of the PV system due to its ASS nature.

The upper limit of the perturbation step-size ΔD_{max} is chosen as 0.5 (thumb rule) and lower limit ΔD_{min} can be selected based on the steady-state performance and the resolution of the ADC (analog to digital converter) used in the microcontroller for realizing the algorithm [69]. The lower value of perturbation step-size $\Delta D_{min} = 0.005$ is considered in this work. The value of ΔD will remain between ΔD_{min} and ΔD_{max}. The limiting values of ΔD can be taken care of by the following condition.

$$\Delta D = \begin{cases} \Delta D_{max}, & \text{if } \Delta D > \Delta D_{max} \\ \Delta D, & \text{if } \Delta D_{max} \leq \Delta D \leq \Delta D_{min} \\ \Delta D_{min}, & \text{if } \Delta D < \Delta D_{min} \end{cases} \tag{3.29}$$

The flow-chart of the proposed current sensor based algorithm is given in Fig. 3.6. It can be seen that only the PV current I_{pv} is sensed through the current sensor and thereby switching function is calculated.

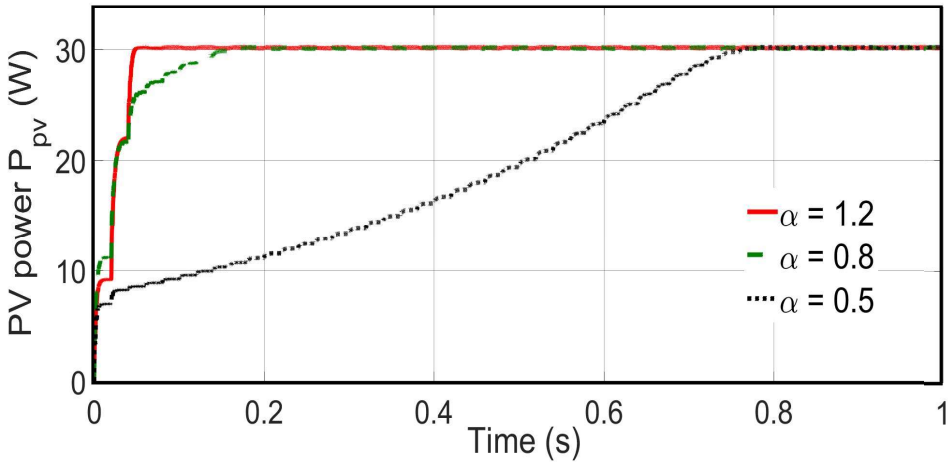

Figure 3.5: PV power P_{pv} for different values of α.

3.4 Design of the SEPIC Converter

In this chapter, a SEPIC converter is used as an interface between the PV module and the resistive load as shown in Fig. 4.1. One advantage of this converter is that, it isolates the input and the output by using coupling capacitor C_1 [94]. The capacitor C_1 protects

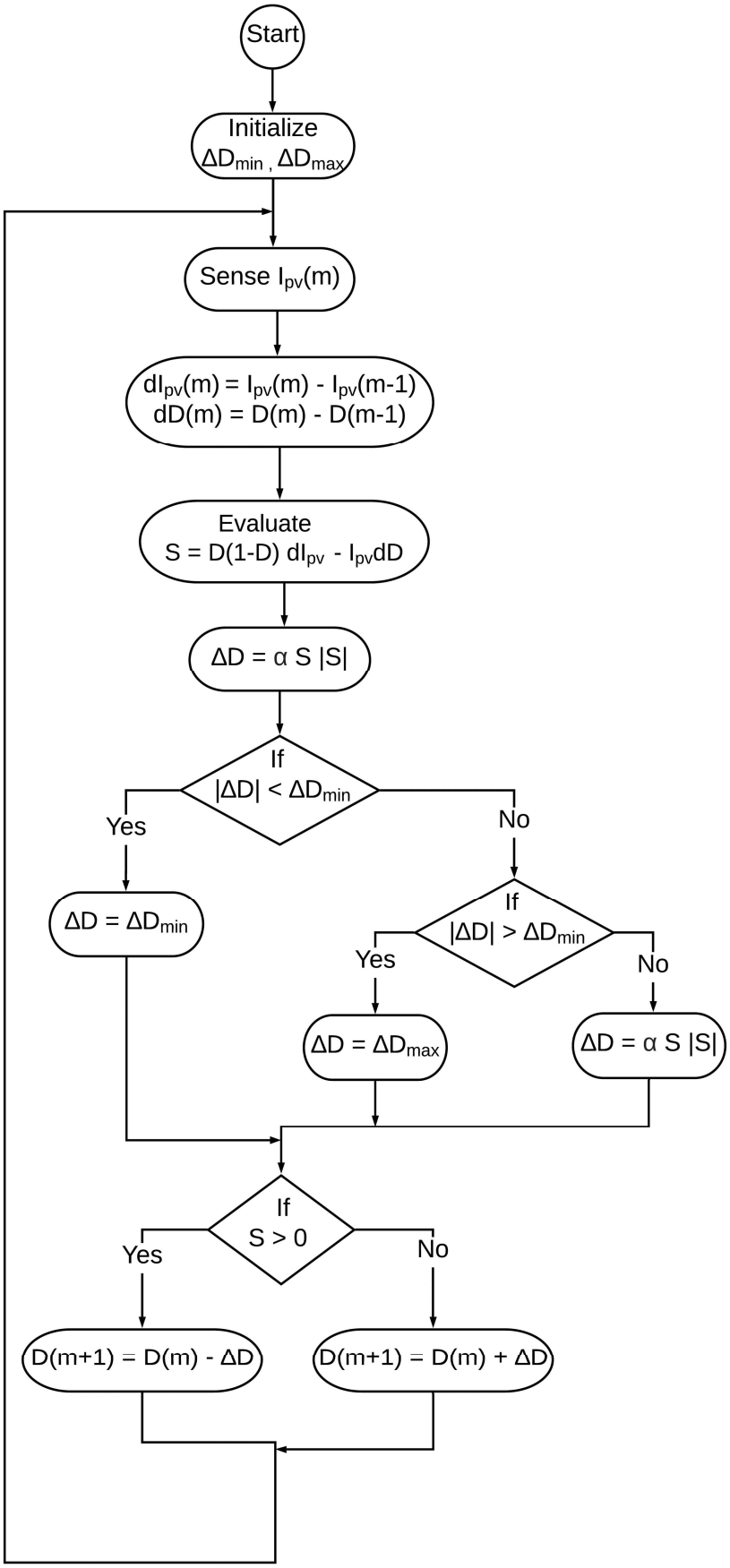

Figure 3.6: Flow-chart of CSB MPPT Technique with adaptive step-size.

against overload and short circuit condition. In this chapter the SEPIC converter is designed [95] for a 40 Watt PV module. The design consideration for the converter is given in Table 4.1.

3.4.1 Duty-Cycle Consideration

For continuous conduction mode (CCM) operation of the SEPIC converter, the maximum duty-cycle is calculated by

$$D_{max} = \frac{V_L + V_D}{V_{pv(min)} + V_L + V_D} \tag{3.30}$$

By putting all the values in (3.30), one gets

$$D_{max} = 0.641 \approx 0.64 \tag{3.31}$$

Table 3.1: SEPIC converter design consideration.

Parameters	**Variables**	**Values**
PV voltage	$V_{pv(min)}$ & $V_{pv(max)}$	10 V & 17.4 V
Load voltage	V_L	17.4 V
Load current	I_L	2.3 A
Voltage drop across diode	V_D	0.5 V
Switching frequency	f_s	50 kHz
Load resistance	R_L	5 Ω

3.4.2 Inductor Selection

Conventionally, the peak to peak ripple current is considered to be 20 to 40 % of the maximum input current I_{pv} at the minimum input voltage $V_{pv(min)}$. Here, the peak to peak ripple current is considered to be 20 %. The ripple current flowing in L_1 and L_2 can be calculated as:

$$\Delta I_L = I_{pv} \times 20\% = I_L \times \frac{V_L}{V_{pv(min)}} \times 20\% \tag{3.32}$$

By putting all the values in (3.32), one gets

$$\Delta I_L = \ 0.8004\ A \approx \ 0.8\ A \tag{3.33}$$

Thereby, the value of inductor is chosen for CCM operation as:

$$L_1 = \ L_2 \geq \frac{V_{pv(min)}}{\Delta I_L \times f_s} \times D_{max} \tag{3.34}$$

By putting the value of ΔI_L from (3.33) into (3.34), we get the values of inductors as:

$$L_1 = \ L_2 \geq 160\ \mu H \tag{3.35}$$

In this chapter the value of inductor $L_{in} = \ L_o = 180\ \mu H$ is chosen for simulation and experimental validation.

3.4.3 Output capacitor selection

The value of output capacitor is calculated by considering the output voltage ripple $V_{ro} = 0.3\ V$

$$C_o \geq \frac{I_L \times D_{max}}{V_{ro} \times 0.5 \times f_s} \tag{3.36}$$

$$C_o \geq 196\ \mu F \tag{3.37}$$

The value of $C_o = 220\ \mu F$ is selected for proposed SEPIC converter.

3.4.4 Coupling Capacitor Selection

The value of coupling capacitor C_1 is calculated by considering the ripple voltage on C_1 as $V_r = 1.3\ V$. Then

$$C_1 = \frac{I_L \times D_{max}}{V_r \times 0.5 \times f_s} \tag{3.38}$$

$$C_1 = 45.29\ \mu F \tag{3.39}$$

The coupling capacitor $C_1 = 47\ \mu F$ is selected which meets the RMS current requirement that produce the small ripple voltage on C_1.

3.4.5 Input Capacitor Selection

The inductor L_1 is connected at the input side of the SEPIC converter. Due to this inductor the input current waveform is triangular and continuous. The inductor makes sure that the current passes through the input capacitor C_1 must have low ripples. The RMS current in the input capacitor is given by

$$I_{C_1(rms)} = \frac{\Delta I_L}{\sqrt{12}} \tag{3.40}$$

The input capacitor C_{in} is selected based on the RMS current handling capability. Although in SEPIC converter C_1 is not so critical, a considerable capacitor value C_2 = 440 μF or higher would prevent impedance interactions with input supply.

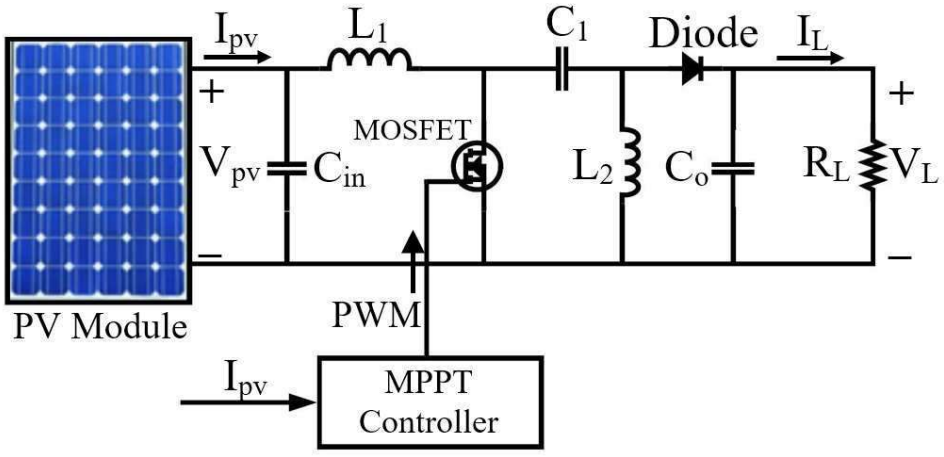

Figure 3.7: Circuit model of PV system with MPPT.

3.5 Simulation Results

The PV module model number ELDROA 40P in MATLAB Simulink [20] is used for simulation of the PV system as given in Fig. 4.1 and MATLAB function block is used for programming of proposed algorithm. The electrical parameters of this module are V_{oc} = 21.9 V, I_{sc} = 2.45 A, V_{mpp} = 17.4 V and I_{mpp} = 2.3 A. The SEPIC converter used in the simulation has the components as follows: L_1 = 180 μH, L_2 = 180 μH, C_1 = 440 μF, C_1 = 47 μF, C_o = 220 μF, load R_L = 5 Ω, and switching frequency f_s = 50 kHz.

3.5.1 Comparison Between Fixed And Adaptive Step-Size

The proposed MPPT technique is first verified by considering FSS (ΔD) = 0.005 and sampling time (T_s) = 20 ms, whereas ΔD_{min} = 0.005 is chosen for ASS technique [36]. The tracking performance for a decrease in insolation from 800 W/m^2 to 500 W/m^2 at 1 s with the FSS and ASS techniques are shown in Fig. 3.8. The variation in PV current with respect to the change in insolation is shown in Fig. 3.8 (a). It is clear that both the techniques are effectively converges to the MPP, but the convergence time is quite large with the FSS (ΔD) = 0.005 technique. It can also be seen that the convergence time with the FSS technique during transient period for G = 800 W/m^2 is T_1 = 720 ms, and the convergence time is reduced to T_1 = 60 ms for the adaptive technique. Similarly, the convergence time T_2 is reduced to 112 ms from 278 ms with the ASS technique as compared to the FSS technique for a decrease in insolation from G = 800 W/m^2 to 500 W/m^2 at 1 s. The corresponding PV voltage and PV power are shown in Fig. 3.8 (b) and (c), respectively. From PV power waveform, it can be observed that the steady-state oscillation is less, hence the steady-state power loss is reduced. From Fig. 3.8 (d), it can be seen that D is oscillating between two-levels at steady-state, and due to this the power loss is less compared to the three level method such as P&O as it is shown in [36]. From the tracking performance given in Fig. 3.8, it can be noticed that both the transient and the steady-state responses are improved for the proposed ASS technique.

3.5.2 Comparison Between Current And Voltage Sensor Based (VSB) MPPT Techniques

In [36], a VSB MPPT technique is proposed for the SEPIC converter. In this method, only PV module voltage V_{pv} is sensed for MPP tracking and the switching function (Q) has been derived in (3.41) to implement this algorithm, where

$$Q = [D(1-D)dV_{pv} + V_{pv}dD] \begin{cases} > 0, \text{on left of MPP} \\ = 0, \text{at MPP} \\ < 0, \text{on right of MPP} \end{cases} \tag{3.41}$$

For both the voltage and the current sensor based MPPT, the following operating conditions are considered: FSS ΔD = 0.005, insolation G = 800 W/m^2. From Figs. 3.9

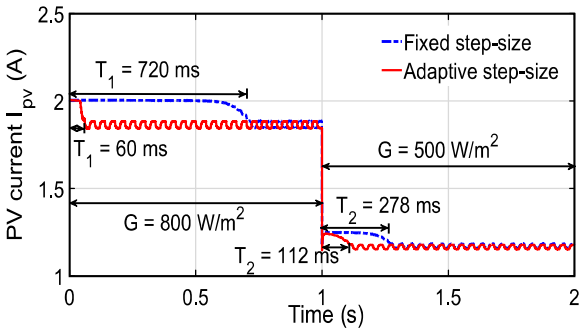

(a)

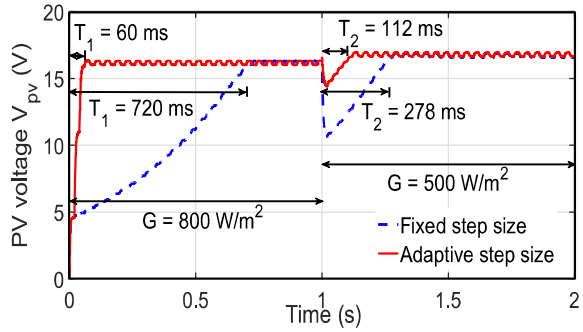

(b)

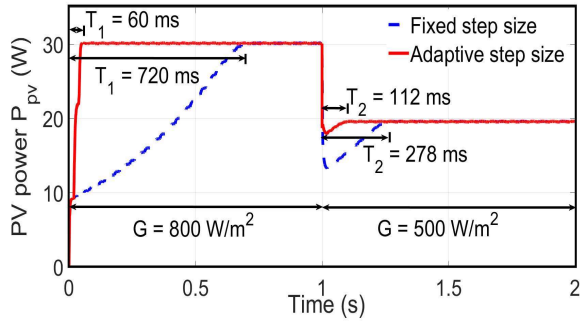

(c)

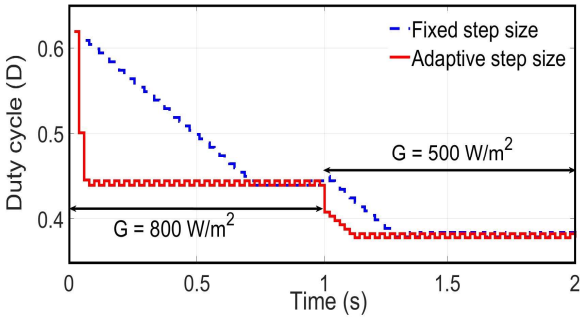

(d)

Figure 3.8: Convergence response of CSB MPPT technique using fixed and adaptive step-size with resistive load. (a) PV Current I_{pv} (b) PV Voltage V_{pv} (c) PV Power P_{pv} (d) Duty cycle D

(a), and (b), it can be observed that the oscillations around MPP at steady-state is much smaller for current sensor based MPPT compared to the VSB one. For the current sensor based one, the power level is always above 30.1 W, whereas for the voltage based one, the power level goes much bellow to 30.1 W. The comparison of dynamic performance of both the MPPT techniques for the same operating condition is shown in Fig. 3.10. The MPP convergence time of current sensor based technique is $T_i = 720\ ms$ which is smaller than the convergence time of VSB technique $T_v = 780\ ms$. It is observed that the current sensor based technique is faster than the VSB technique.

Fig. 3.11 shows a comparison of S and Q variation with respect to D. From Fig. 3.11, it can be observed that the switching function S (for the current sensor) is more regular around the MPP with a saturation characteristic visible. Moreover, it is considerably uniform (large constant value) on the right side of the MPP in comparison to the irregular variation in Q (for voltage based). Hence, it is expected that the switching function S will work better than Q for large change in insolation.

3.5.3 Simulation Results with Different Operating Conditions

The simulation results with different loads are shown in Figs. 3.12 and 3.13 for uniform insolation level $G = 800\ W/m^2$ and temperature $T_{emp} = 43\ ^oC$. The generated PV power shown in Fig. 3.12 is same for all the loads. It is also clear that the proposed CSB technique is able to track the MPP for different load conditions and the MPP convergence time is same irrespective of the loads. From Fig. 3.13, it is clear that the load power P_o is different for all the loads. The load power increases with increase in the load resistance due to the varying efficiency of the converter. For series RL and parallel RC loads, the PV power variations are shown in Fig. 3.14. It is clear that, for both the RL and RC loads,responses are same as the resistive one in Fig. 3.12. However there are small changes in the transient response, though the settling times are almost similar.

The simulation result with variable temperature is given in Fig. 3.15 for uniform insolation level $G = 800\ W/m^2$. Any PV module generates maximum power at standard test condition ($G = 1000\ W/m^2$ and temperature $T_{emp} = 25\ ^oC$). It can be observed that the PV power P_{pv} increases with decrease in temperature.

The proposed CSB MPPT technique is also studied for different switching frequencies and the resulted PV power is shown in Fig. 3.16. It can be observed that the PV power is

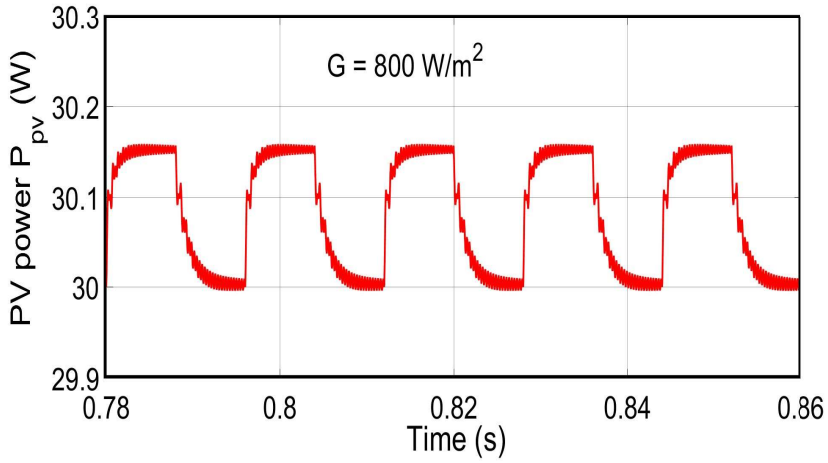

(a)

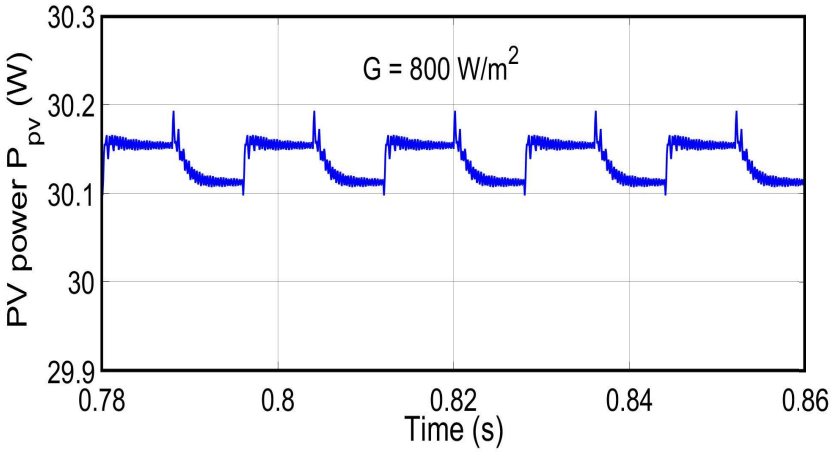

(b)

Figure 3.9: PV power P_{pv} at steady-state. (a) Voltage sensor based MPPT. (b) Current sensor based MPPT.

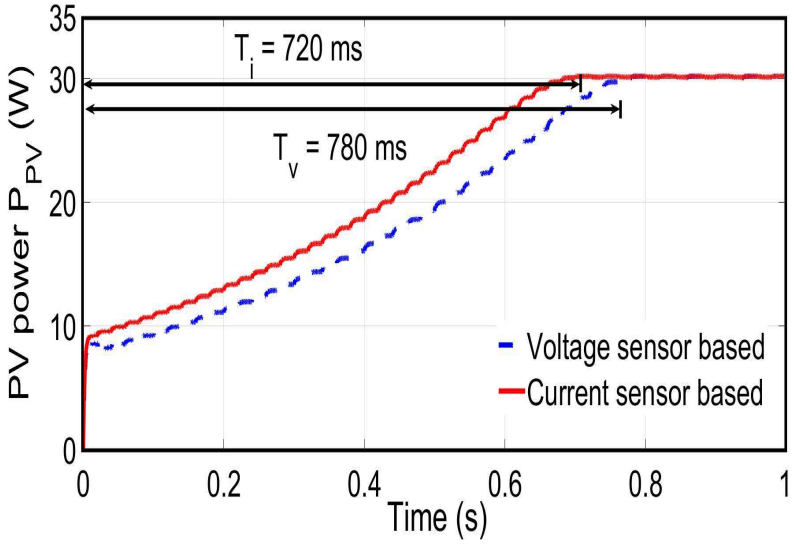

Figure 3.10: Comparison of dynamic performance at $G = 800\ W/m^2$.

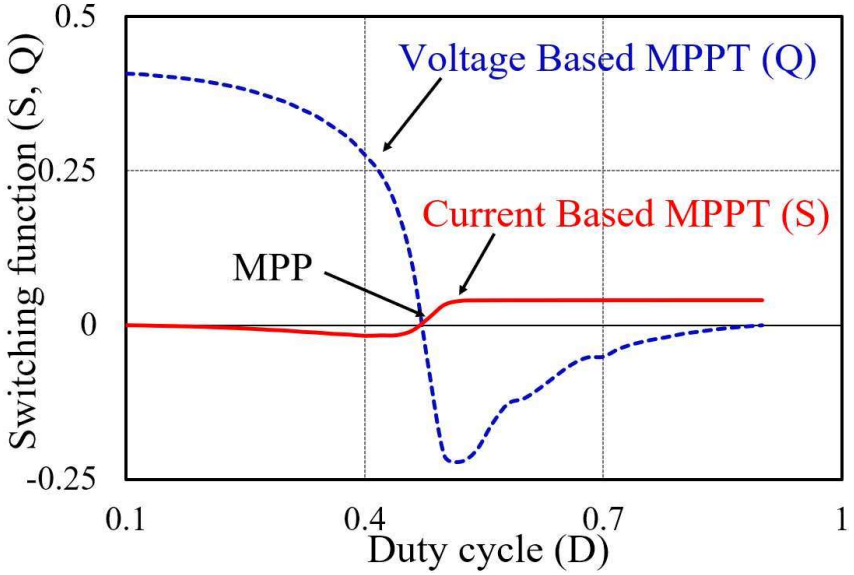

Figure 3.11: Switching functions vs duty-cycle $(S, Q - D)$ characteristics.

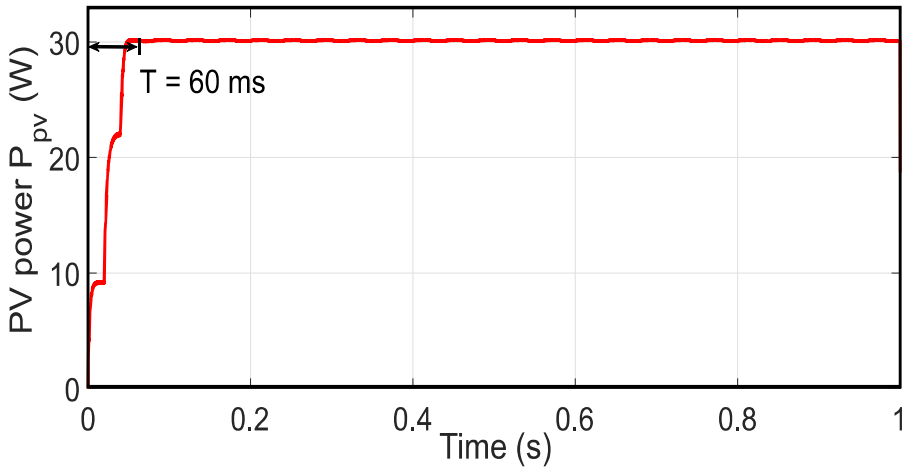

Figure 3.12: PV power P_{pv} with different loads.

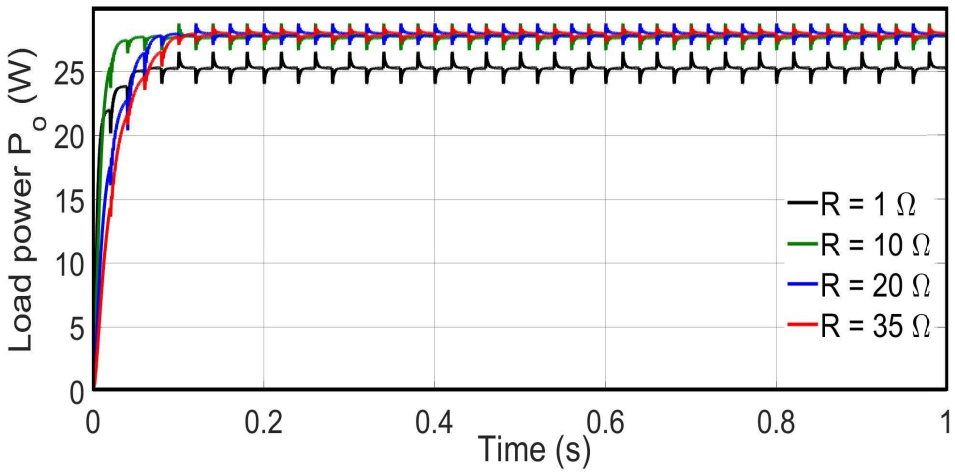

Figure 3.13: Load power P_o with different loads.

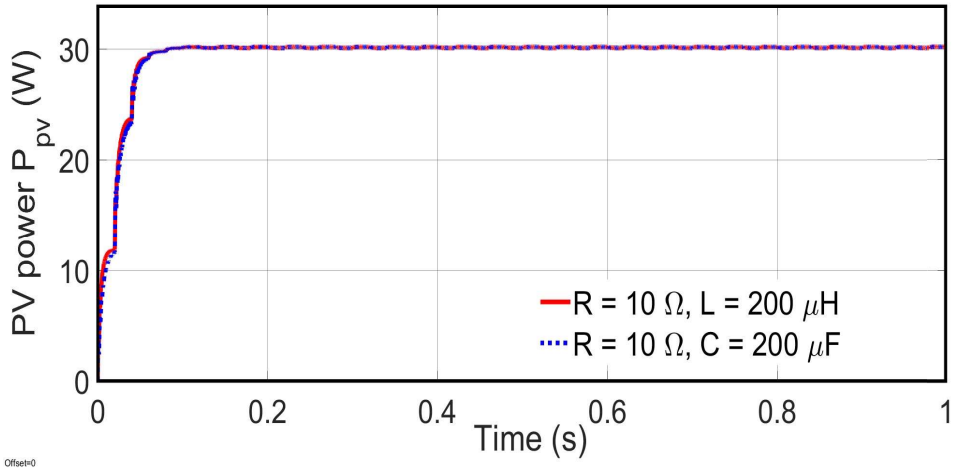

Figure 3.14: PV power P_{pv} with RL and RC loads.

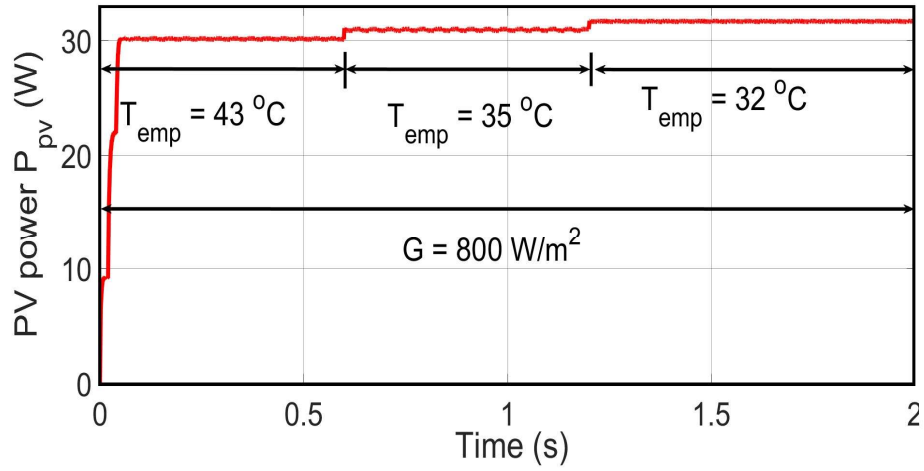

Figure 3.15: PV power P_{pv} with variable temperature.

almost same for these frequencies. The average PV power is different due to oscillations around the MPP at the steady-state.

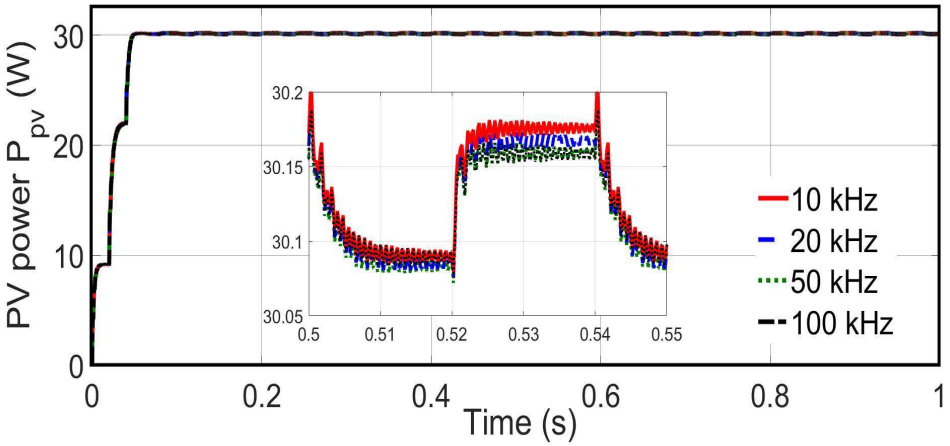

Figure 3.16: PV power P_{pv} with different switching frequencies.

3.5.4 Performance Comparison

A performance comparison with a recent technique [94] that uses SEPIC converter and adaptive technique step-size is made in this section. Note that results in [94] considered SEPIC converter for impedance matching, adaptive nature of step-size and tested for change in insolation-levels, that are similar to the method adopted in this chapter. The only difference between the work in this chapter and [94] is the MPPT algorithm. This technique in [94] based on two fixed step-size, one is large step-size ΔD_{LS} and other

is small step-size ΔD_{SS}. Two step-sizes are considered for the adaptation purpose. A large step-size is chosen when the operating point is far from the MPP, say area A, to improve the MPP tracking time, and small step-size is considered when the operating point nearing the MPP, say area B, to reduce the oscillation at steady-state. Hence, this is not a true adaptive MPPT technique. The operating area B is detected by the following condition [94]:

$$\left|\frac{\Delta P_{pv}}{\Delta V_{pv}}\right| \leq Z \tag{3.42}$$

Another important condition is defined to detect large variation in either load or insolation as [94]:

$$\frac{\Delta I_{pv}}{\Delta V_{pv}} + \frac{I_{pv}}{V_{pv}} < E \tag{3.43}$$

In this chapter, for the sake of comparison, the result of [94] is also simulated with Z = 1.64 and E = 0.1092 calculated from (4.15) and (3.43), respectively, for change in insolation level from G = 0 to 800 W/m^2. The large step-size ΔD_{LS} = 0.03 and small step-size ΔD_{SS} = 0.005 are considered. The PV power convergence responses for enhanced auto-scaling incremental conductance (EAS IncCond) MPPT [94] and CSB MPPT with adaptive step-size (ASS) are shown in Fig. 3.17, it can be seen that the MPP convergence time for EAS IncCond technique $T_2 = 140\ ms$, which is larger than the convergence time for CSB (ASS) technique $T_1 = 60\ ms$. This is due to the fixed step-size (though overall adaptive) used for the transient period, hence the convergence depends on how large large step-size is chosen. From Fig. 3.18, it can be seen that the EAS IncCond MPPT technique has three-level operation around MPP, whereas with the proposed technique have two-level operation. It is shown in [36] that two-level operation is beneficial. Due to this, the oscillation around MPP in PV power is less with the proposed technique as compared to the EAS IncCond technique and this can be seen in Fig. 3.17.

Next, a comparison of efficiencies is made. The average MPP tracking efficiency $\eta_{mpp(avg)}$ is calculated as [94]:

$$\eta_{mpp(avg)} = \frac{P_{mpp(avg)}}{P^*_{mpp(avg)}} \times 100 \tag{3.44}$$

where $P_{mpp(avg)}$ is the extracted average maximum power from the PV module. $P^*_{mpp(avg)}$ is the available average maximum PV power. For insolation level G = 800 W/m^2, it is 30.28 W. The PV power reaches at steady-state after time t = 0.14 s for both the techniques as shown in Fig. 3.17. Hence, the values of $P_{mpp(avg)}$ and the corresponding

average efficiencies $\eta_{mpp(avg)}$ are calculated for the time ranges $t = 0$ to 0.2 s and $t = 0.2$ to 1.0 s to differentiate between the transient and steady-state efficiencies as shown in Table 3.2. It can be observed that the average efficiency is improved with the proposed adaptive step-size CSB MPPT technique considerably during transient-state, whereas the average efficiency is almost similar at steady-state since the small step-size ΔD_{SS} and minimum step-size ΔD_{min} are same for the two techniques.

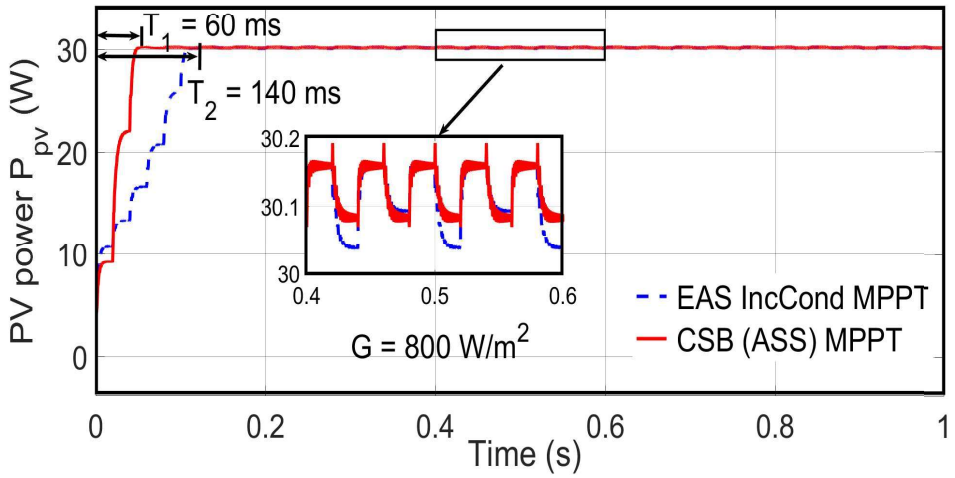

Figure 3.17: Comparison of adaptive current sensor based MPPT technique and enhanced auto scaling IncCond MPPT technique with resistive load.

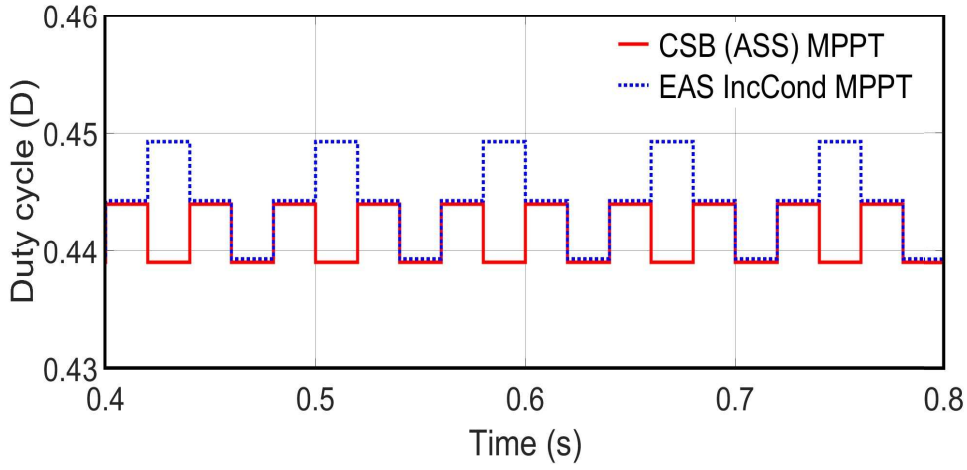

Figure 3.18: Comparison of duty-cycle at steady state for CSB (ASS) MPPT and EAS IncCond MPPT techniques.

A comparison of PV power for CSB (ASS) MPPT technique and EAS IncCond MPPT technique with battery load (12 V, 7 Ah) is shown in Fig. 3.19. It can be observed

Table 3.2: Comparison of CSB (ASS) MPPT with enhanced auto scaling IncCond MPPT technique.

Parameters	**EAS IncCond [94]**	**CSB (ASS)**
Sensors	Voltage (V) & Current (I)	Current (I)
Steady state operation	3-Level	2-Level
Complexity	Medium	Low
Adaptive step-size ΔD	$\Delta D_{LS} = 0.03$ & $\Delta D_{SS} = 0.005$	$\alpha\ S\ \lvert S \rvert$
Convergence time	$T_2 = 140\ ms$	$T_1 = 60\ ms$
$P_{mpp(avg)}$ (0 - 0.2 s)	23.4054 W	26.8450 W
$\eta_{mpp(avg)}$ (0 - 0.2 s)	77.30 %	88.65 %
$P_{mpp(avg)}$ (0.2 - 1 s)	30.1174 W	30.1968 W
$\eta_{mpp(avg)}$ (0.2 - 1 s)	99.46 %	99.73 %

that the MPP convergence times $T_1 = 40\ ms$ and $T_2 = 100\ ms$ with battery load are reduced as compared to the convergence time with resistive load shown in Fig. 3.17. This is because the SEPIC converter works in buck-mode as the battery voltage is less than the V_{mpp}. Hence the average tracking efficiencies are improved at transient-state due to the reduced tracking time and almost similar at steady-state as compared to resistive load. This shows that the proposed MPPT technique performs well for battery load as well.

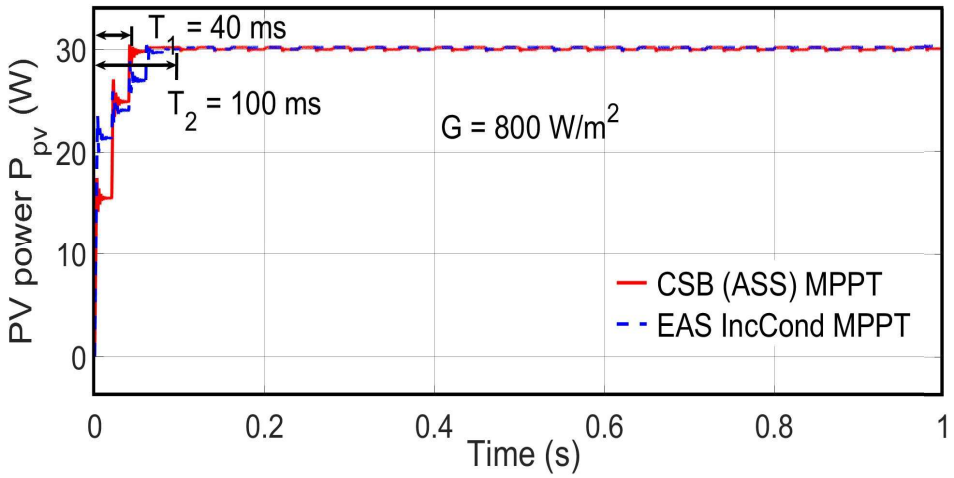

Figure 3.19: Comparison of adaptive current sensor based MPPT technique and enhanced auto scaling IncCond MPPT technique with battery load.

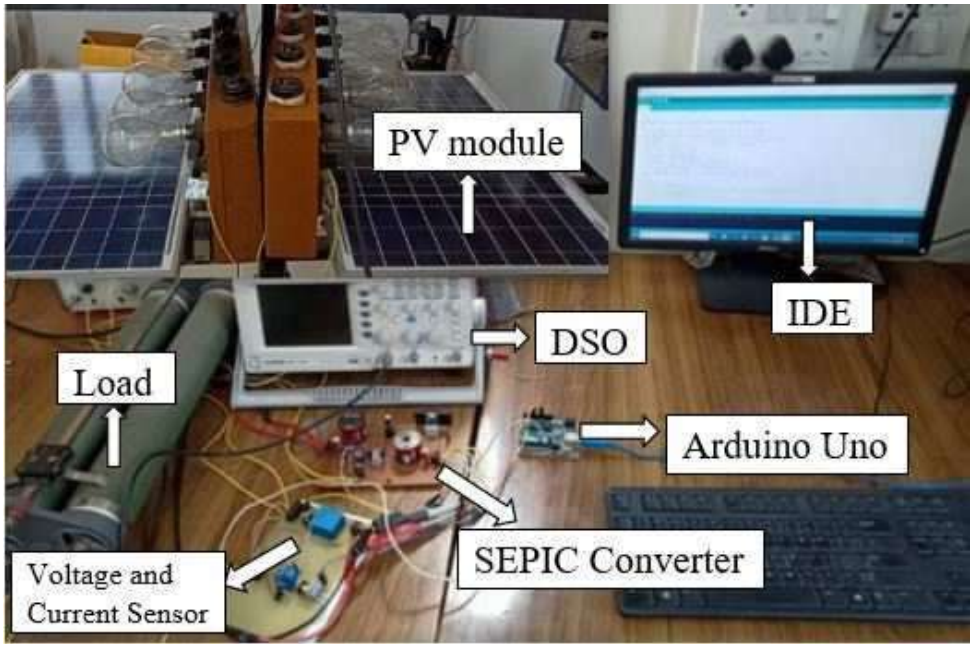

Figure 3.20: Experimental model of the PV system.

3.6 Experimental Setup And Validation

To verify the tracking performance and functionality of the current sensor based technique, an experimental model of the SEPIC converter with controller circuit is designed in laboratory. The converter have the same parameters as given in Section 3.5. An ARDUINO UNO controller has been considered for implementation of the proposed technique and to provide the desired switching signal to the converter. The experimental setup of the PV system is shown in Fig. 4.14.

To implement the current sensor based technique, current measurement is required. The current is measured using LEM LTS6-NP hall effect current transducer. An IRFIZ44N power MOSFET, STPS2045CT power Schottky diode and HCPL3120 gate driver ICs are used for SEPIC converter design. An ELDORA 40P PV model having the same parameters as given in Section 3.5 is used to perform the experiment and halogen lamps are used for artificial insolation. The insolation of light is controlled by manual switches and the insolation is measured by using the solar power meter WACO 206.

The current sensor based MPPT technique with the fixed and ASS techniques are compared for a change in insolation. The start-up tracking performance with the FSS technique at approximately $G = 800\ W/m^2$ is given in Fig. 3.21 (a), and it can be noticed that the start-up convergence time is $T_1 = 2500\ ms$. The tracking performance with the

FSS technique for a change in solar insolation level approximately from G = 500 W/m^2 to 800 W/m^2 and from $G = 800\ W/m^2$ to 500 W/m^2 are given in Fig. 3.21 (b) and (c), respectively. It can be observed that the convergence time to reach at MPP are $T_2 = 2000\ ms$ and $T_3 = 1300\ ms$, respectively. Similarly, the tracking performance with ASS technique corresponding to start-up and change in solar insolation levels approximately from $G = 500\ W/m^2$ to 800 W/m^2 and from $G = 800\ W/m^2$ to 500 W/m^2 are shown in Fig. 3.22 (a), (b) and (c), respectively. From Fig. 3.22, it can be observed that the convergence time T_1 is reduced to 1000 ms from 2500 ms, T_2 is reduced to 600 ms from 2000 ms and T_3 is reduced to 550 ms from 1300 ms with the ASS technique compared to the FSS technique. Thus, the ASS technique is effective in terms of reduced convergence time.

For evaluation of the steady-state performance of the proposed technique, experiments are performed with sampling time $T_s = 1\ s$, and the corresponding waveforms are shown in Fig. 3.23. It can be observed that the proposed MPPT technique is giving two-level operation during steady-state, which effectively reduces the steady-state power loss as compared to EAS IncCond technique [36].

The average efficiencies of the experimental results are calculated based on (3.44) and shown in Table 4.3, where the value of $P^*_{mpp(avg)}$ is 30.28 W for the insolation-level 800 W/m^2. From Figs. 3.21 (a) and 3.22 (a), it is clear that the PV voltage and the current reach steady-state after time $T_1 = 2.5\ s$. Hence the average extracted maximum powers $P_{mpp(avg)}$ and the corresponding average efficiencies $\eta_{mpp(avg)}$ is calculated for the two time ranges, one for 0 to 2.6 s and the other for 2.6 to 9 s to differentiate the transient and steady-state efficiencies as shown in Table 4.3. It can be observed that the efficiency $\eta_{mpp(avg)}$ is considerably improved with the proposed adaptive step-size algorithm during both the transient and steady-state as compared to the fixed step-size one. However, it may be noted that the efficiency calculated here is based on true insolation-level of 800 W/m^2 though actual insolation-level may vary since the environmental condition is not ideal in the experimental setup. The efficiencies tabulated are just indicative for comparison of the two methods and does not indicate absolute efficiency of the system.

Experiments are also performed for lead-acid battery load (12 V, 7 Ah) using CSB technique with ASS and EAS IncCond [94] technique, and the corresponding convergence responses for change in insolation-level from 0 to 800 W/m^2 are shown in Figs. 3.24 and

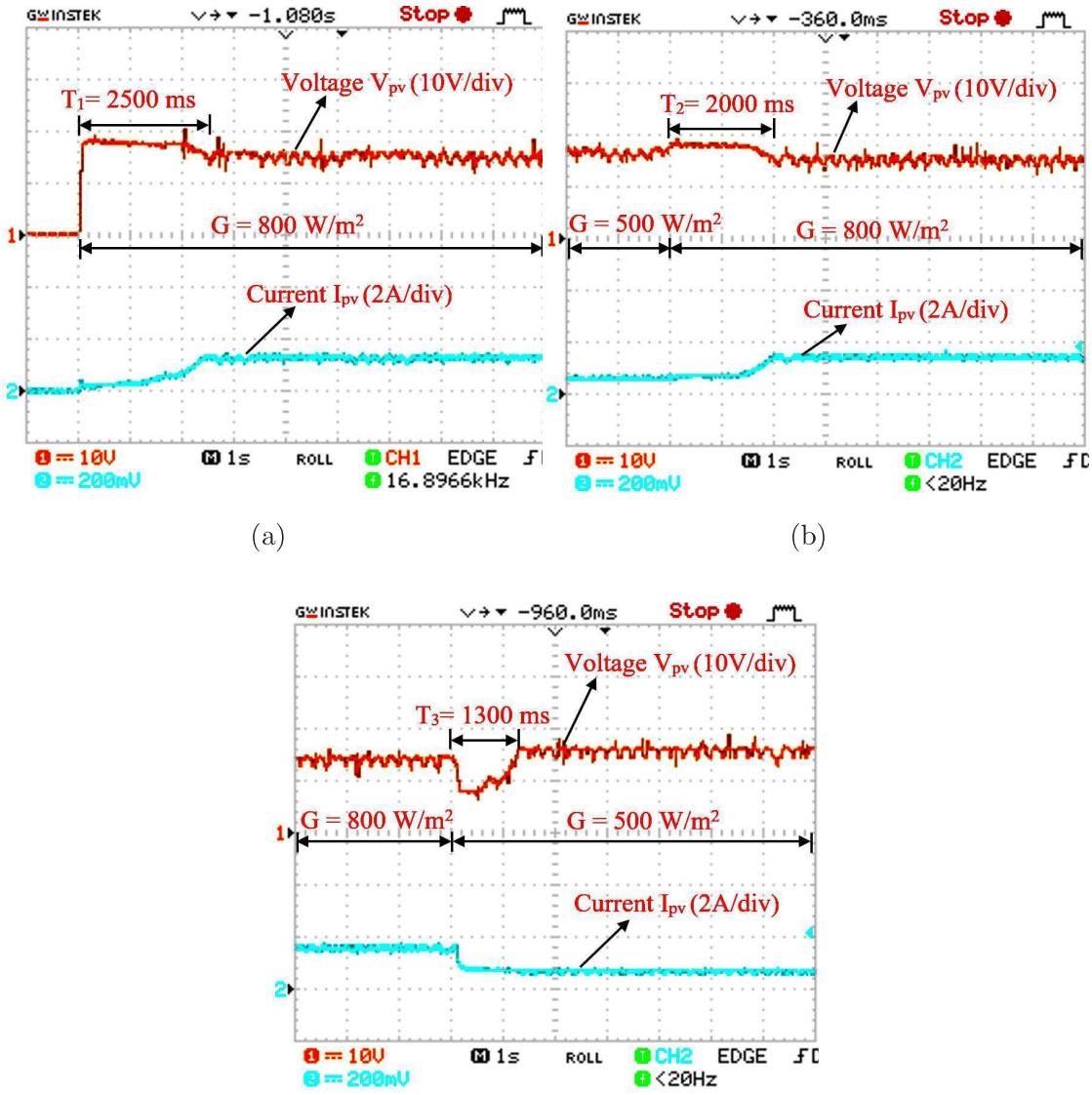

Figure 3.21: Convergence response of CSB MPPT technique using FSS with resistive load. (a) start-up at $G = 800\ W/m^2$ (b) for increase in insolation level (c) for decrease in insolation level.

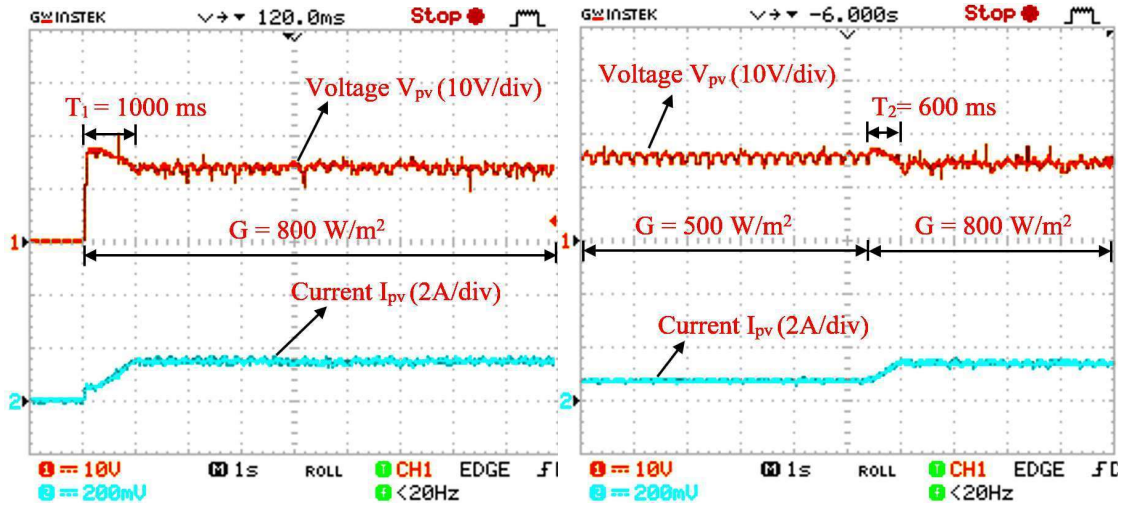

(a) (b)

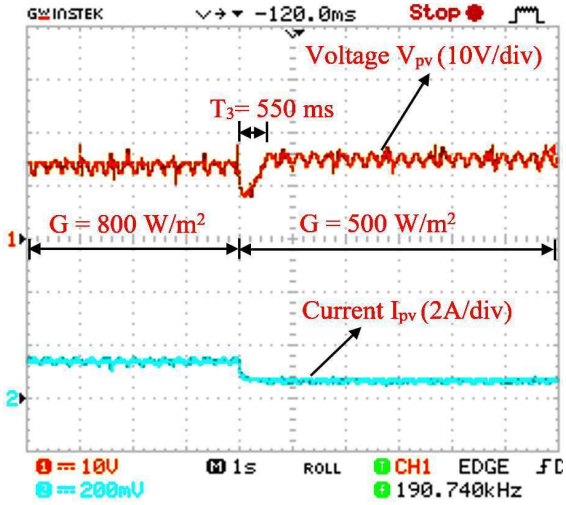

(c)

Figure 3.22: Convergence response of CSB MPPT technique using ASS with resistive load. (a) start-up at $G = 800\ W/m^2$ (b) for increase in insolation level (c) for decrease in insolation level.

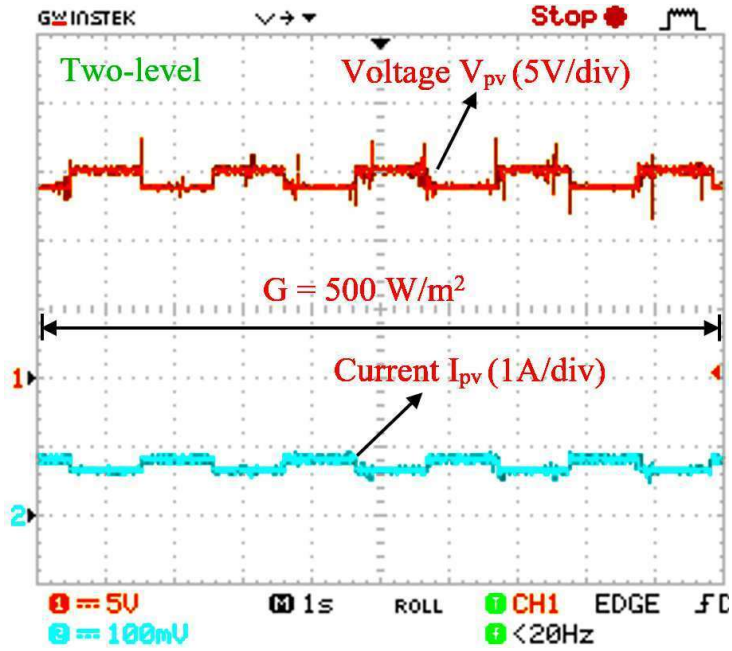

Figure 3.23: Two level operation at steady-state for G = 500 W/m^2 with CSB (ASS) MPPT Technique using $T_s = 1\ s$

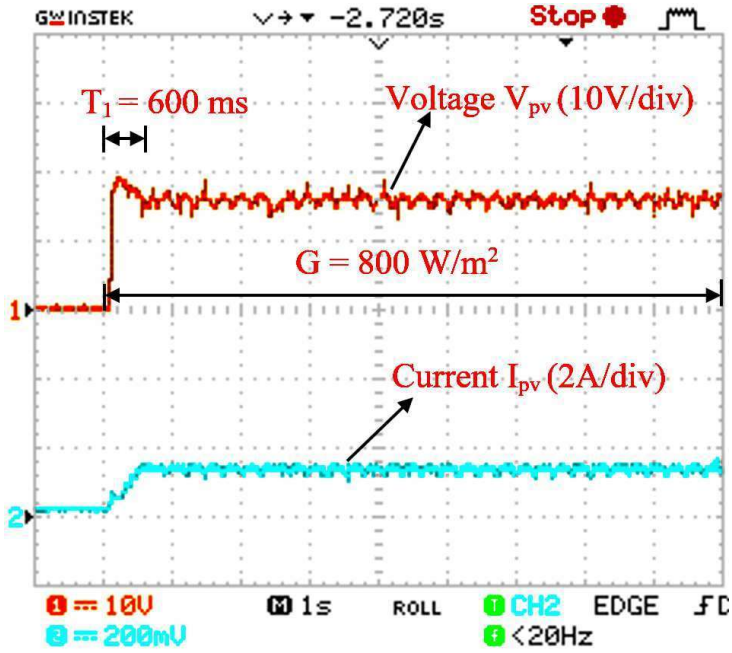

Figure 3.24: Convergence response of CSB (ASS) MPPT technique with battery load for start-up at $G = 800\ W/m^2$.

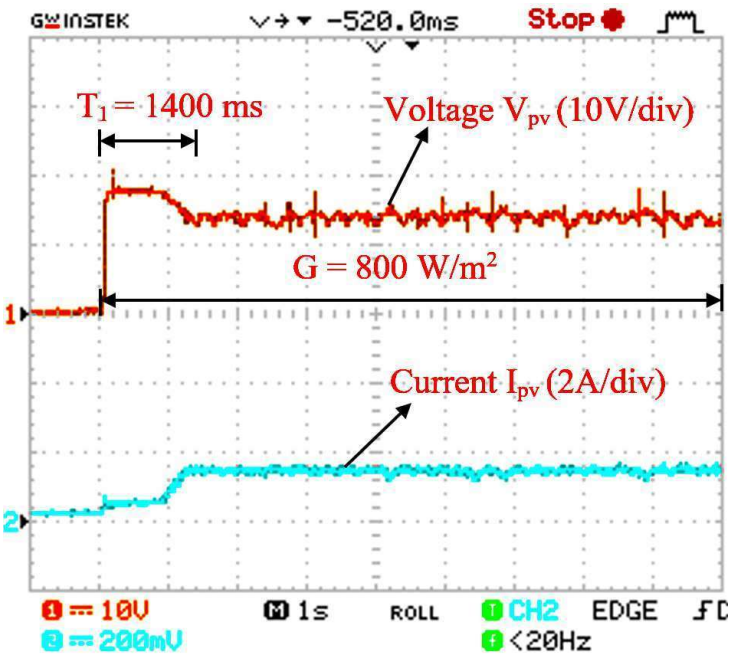

Figure 3.25: Convergence response of EAS IncCond MPPT technique with battery load for start-up at $G = 800\ W/m^2$.

3.25, respectively. It is clear that both the techniques are effectively tracking the MPP point with the battery load. The SEPIC converter always operates in buck mode, because the rated battery voltage is less than the maximum power point voltage (V_{mpp}). Hence, the variation in the duty-cycle is less for change in insolation level, due to which the MPP convergence time (600 ms) is reduced with the battery load as compared to the resistive load (1000 ms). The average tracking efficiencies are also calculated for the results shown in Figs. 3.24 and 3.25 for the two time ranges as shown in Table 4.2. It can be observed that the efficiencies for resistive load and battery load are almost similar for both the time ranges. Hence, the proposed technique improves the performance for battery load as well. The comparison of simulation and experimental results using CSB (ASS) MPPT technique are shown in Table 3.5.

Table 3.3: Comparison of experimental results of CSB MPPT technique using fixed and adaptive step-size with resistive load.

Parameters	**CSB (FSS)**	**CSB (ASS)**
Convergence time T_1 (0 - 800 W/m^2)	2500 ms	1000 ms
Convergence time T_2 (500 - 800 W/m^2)	2000 ms	600 ms
Convergence time T_3 (800 - 500 W/m^2)	1300 ms	550 ms
$P_{mpp(avg)}$ (0 - 2.6 s)	21.8357 W	24.9187 W
$\eta_{mpp(avg)}$ (0 - 2.6 s)	72.11 %	82.29 %
$P_{mpp(avg)}$ (2.6 - 9 s)	27.9017 W	27.9185 W
$\eta_{mpp(avg)}$ (2.6 - 9 s)	92.14 %	92.20 %

Table 3.4: Comparison of experimental results of CSB MPPT technique using adaptive step-size and EAS IncCond with battery load.

Parameters	**EAS IncCond**	**CSB (ASS)**
Convergence time T_1 (0 - 800 W/m^2)	1400 ms	600 ms
$P_{mpp(avg)}$ (0 - 2.6 s)	24.4610 W	26.6947 W
$\eta_{mpp(avg)}$ (0 - 2.6 s)	80.78 %	88.16 %
$P_{mpp(avg)}$ (2.6 - 9 s)	27.8694 W	27.9067 W
$\eta_{mpp(avg)}$ (2.6 - 9 s)	92.04 %	92.16 %

Table 3.5: Comparison of simulation and experimental results of CSB MPPT technique using adaptive step-size with resistive load.

Parameters	**Simulation**	**Experimental**
Convergence time (0 - 800 W/m^2)	60 ms	1000 ms
Convergence time (800 - 500 W/m^2)	112 ms	550 ms
$P_{mpp(avg)}$ (Steady-state)	30.1968 W	27.9185 W
$\eta_{mpp(avg)}$ (Steady-state)	99.73 %	92.20 %

In chapter 4 , analysis of load voltage based MPPT technique, proposed load voltage based MPPT technique with fixed and adaptive step-size, design of SEPIC converter, and transient analysis of $V_L - D$ characteristics of PV module are described and the developed MPPT technique is validated through MATLAB simulation and experimental results.